Study on the Vibration Reduction Characteristics of FWMAV Flexible Bionic Wings Mimicking the Hindwings of *Trypoxylus dichotomus*

Yongwei Yan[1] · Fa Song[1] · Nuo Xu[1] · Haochen Zhu[1] · Hongxu Xing[1] · Shujun Zhang[1,2] · Jiyu Sun[1]

Abstract

Using the method of structural finite element topology optimization and analysis of the hindwings of *Trypoxylus dichotomus*, this work identified the main loading force transmission path and designed the initial structure of a bionic flexible wing. A structural design scheme of the vibration damping unit was proposed, and the structural mechanics and modal vibration characteristics were simulated and analyzed. 3D printing technology was used to manufacture the designed bionic wing skeleton, which was combined with two kinds of wing membrane materials. The Flapping Wing Micro-aerial Vehicle (FWMAV) transmission mechanism vibration characteristics were observed and analyzed by a high-speed digital camera. A triaxial force transducer was used to record the force vibration of the flexible bionic wing flapping in a wind tunnel. A wavelet processing method was used to process and analyze the force signal. The results showed that the force amplitude was more stable, the waveform roughness was the lowest, and the peak shaving phenomenon at the z-axis was the least obvious for the bionic flexible wing model that combined the topology-optimized bionic wing skeleton with a polyamide elastic membrane. This was determined to be the most suitable design scheme for the wings of FWMAVs.

Keywords Vibration reduction characteristics · Bionic wings · Flapping-wing micro-aerial vehicle (FWMAV) · Beetle Hindwings

Shujun Zhang | szhang@glos.ac.uk
*Jiyu Sun | sjy@jlu.edu.cn

[1] Key Laboratory of Bionic Engineering (Ministry of Education, China), Jilin University, Changchun 130022, China
[2] School of Computing and Engineering, Gloucestershire University, Cheltenham GL50 2HR, UK

1 Introduction

Micro-aerial vehicles (MAVs) were first proposed in 1992; these vehicles can be divided into fixed wing, rotor wing, and Flapping Wing MAVs (FWMAVs), have broad application prospects in military and civilian fields and are an active development and high intersection field of research [1, 2]. With the development of advanced manufacturing technology, aerodynamics, and insect flight mechanics, size miniaturization, high power efficiency, lightweight structure, and intelligent control are the main directions of the future development [3, 4].

Compared with traditional fixed wing and rotor wing MAVs, the flight mode of FWMAVs has the best aerodynamic efficiency at low Reynolds numbers, and the anti-interference ability is the strongest, which is an ideal model to adapt to the future development of MAVs [5]. However, the complex periodic harmonic aerodynamic loads generated by FWMAV wings can cause wing flutter and even body chatter, resulting in structural damage and aerodynamic reduction of the wing surface [6].

Thus, these factors seriously affect the flight stability and maneuverability and the performance and service life of FWMAV components [7]. The vibration problem severely restricts the development of FWMAVs and is an urgent problem to be solved at present.
Researchers have studied many of the flapping wing mechanisms of flying animals in nature and proposed a series of unsteady flapping flight theories, such as “clapfling” [8], “delayed stall [9]”, “wake capture [10]”, “rotational circulation [11]”, and “rapid pitch rotation [12]”, among others [13, 14]. However, for flapping wing flight, there is a lack of consensus on how to reduce complex periodic harmonic aerodynamic loads and maintain dynamic stability.

Some researchers have proposed that the elastic deformation of flexible wings can effectively resist the vibration impact of aerodynamic loads on flying animals themselves [15–17]. The flight of an insect is mainly realized by the high-frequency flapping of its wings [18]. The interaction between the aerodynamic force generated by the flapping of the wings and the elastic force easily causes body flutter [19, 20]. The flexible deformation of the wings can prevent vibration over the natural frequency range to avoid wing damage caused by flight interference and resonance of the wings [21]. The natural frequency and stiffness of insect wings also change with torsional deformation during flight, thereby adapting to the force change during flight and reducing the impact of fluctuating loads [22]. The closer the flapping frequency is to the natural frequency, the larger the potential wing variation, which promotes adaptation to flow field changes by flexible deformation and reduces energy consumption [23]. This means that the flexible wing can be flexibly deformed compared with the rigid wing, which helps reduce wing flutter and body chattering while obtaining high lift [22, 24]. Therefore, the flexible vibration characteristics of wings must be considered in the design of FWMAVs.

The active flexible control of wing deformation can be realized by using piezoelectric materials, including wing flutter suppression, gust load mitigation, and chattering suppression [25–27]. The bionic flexible wing skeleton designed according to the beetle hindwing creases has an excellent vibration reduction function. When it collides with an object, it folds along the creases and springs back in the flapping wing cycle. This can effectively reduce the impact of wing collisions in flight and help the aircraft quickly return to normal flight [28]. Using a bionic discrete wing structure designed from bird feathers, under the control of the deformed skeleton structure, the wing skeleton can actively deform and effectively reduce the strength of the wing tip vortex, realize the active drag reduction of aircraft, and improve flight stability [5]. The bionic design of dragonfly wing vein structures based on the topology optimization analysis method can effectively reduce the mass of the bionic wing and enhance its flexible deformation ability [29]. For a bionic wing made by the additive manufacturing method, compared to the hindwing, the first two natural frequencies differ by 7% and 16%, respectively, and the vibration patterns are similar [30]. The first-order natural frequency of the bionic wing is significantly changed when the wing mass is changed [31]. Chen Long et al. used UV-curable resin as the base material for 3D printing, proposed a topology optimization modeling method considering nonlinear factors such as contact, friction and collision, and verified the optimization results through dynamic simulation and experiments, which has certain guiding significance for the lightweight design of flexible MAVs [32].

With the development trend of size miniaturization and lightweight structures, beetles provide a new bionic inspiration for the development of flexible wings [33]. According to the mass and stiffness distribution of the beetle’s hindwing and considering the anisotropy of the hindwing structure, a bionic wing model consisting of wing membranes and conical veins was established. After modal analysis, it was found that the hindwing deformation was conducive to the downward flow of air and generated a higher lift force [34]. Taking the hindwing of the Asian ladybird as the bionic prototype, three hind wing models with different structures were established, and finite element simulation analysis was carried out. Research shows that different vein structures have a great influence on the dynamic stability characteristics [35]. The bionic folding wing, inspired by the hindwing, reduced the risk of wing damage while gaining sufficient lift [36].

The mechanical characteristics of FWMAV wings directly determine the flight stability of FWMAVs. At present, the design and manufacturing method of FWMAV wings is still not perfect; there is no connection between the design and manufacture of wings and the specific vibration characteristics (dynamic stability characteristics) of FWMAVs, and there is no specific theory and method of FWMAV vibration reduction and manufacture. From the perspective of bionics, this study takes the hindwing of the beetle as the bionic prototype, synthetically uses the theories and methods of bionic principle, finite element analysis, vibration analysis, and 3D printing technology to develop a flexible wing suitable for FWMAVs, and analyzes its vibration mechanical characteristics, which will help to study the dynamic stability characteristics of the material to the wings of FWMAVs. This work provides a specific and effective practical reference for the design and manufacture of FWMAV wings.

2 Materials and Methods

2.1 The Hindwing Model and Topology Optimization Analysis

2.1.1 The Beetle and Its Hindwings

T. dichotomus and its hindwings are shown in Fig. 1 and have excellent flight ability and stability. Hindwings are soft and foldable; during flapping flight, flexible deformation and “∞” torsion can be used to obtain high lift and resist the impact of unsteady vortices to reduce vibration [37]. During non-flight, hind wings can be folded under the elytra to reduce the overall size of the insect, facilitate migration, and resist natural enemies. Beetles were acquired from Quanzhou, China, and five males of similar size were selected as subjects.

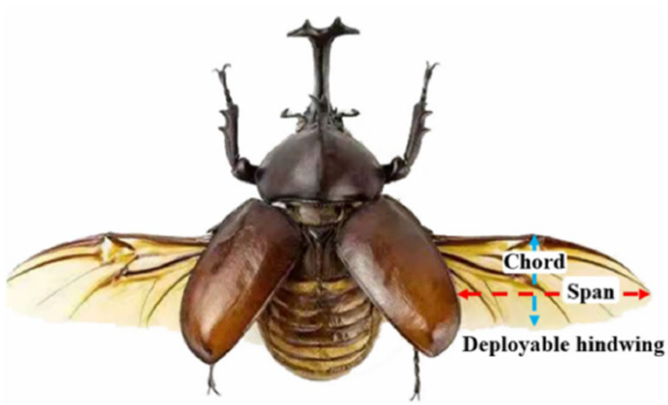

Figure 1 T. dichotomus and its hindwings.

2.1.2 The Hindwing Model and Topology Optimization Analysis

This paper is based on the preliminary work of our research group [38, 39], including measuring the morphological characteristics, establishing a 3D model (Fig. 2a), obtaining nanomechanical material properties, and analyzing the structural mechanical properties of the model. Based on the analysis of the structural mechanical properties of the hindwing model under uniform load and considering the integrity of the wing membrane and the feasibility of 3D printing of the model, after fixing the wing membrane and the wing base (Fig. 2b), topology optimization analysis of the wing veins was carried out (Fig. 2c). According to the calculation results upon replacing the wing base element with the linkage unit that can connect with the FWMAV, a 3D printing model of wing veins was obtained (Fig. 2d).

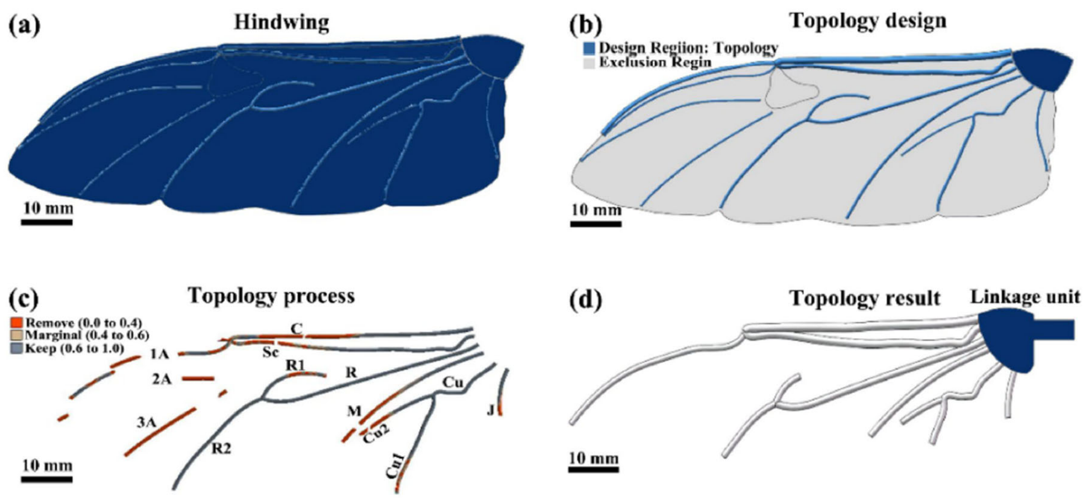

Figure 2 Hindwing model and topology optimization analysis.

The ANSYS Workbench (19.2) was used to analyze and topology optimization of the hindwing model. The parameters of the hindwing model are present in Table 1. The veins were selected as the design area of topology optimization, and the membrane was selected as the non-design area. The base of the hindwing model was constrained, and a uniform load (0.05 N) was applied on it. The response constraint was retained 50% of the mass. The wing membrane and veins were meshed using the automatic method due to their complex geometry, and their minimum mesh sizes were set as 0.5 mm and 0.1 mm, respectively. The number of grids was 293333, which met the requirement of grid computing independence.

Table 1 Parameters used in the hindwing model.

Parameters	Value	Parameters	Value
Hindwing area (mm^2)	847.20 ± 0.05	Beetle weight m (g)	7.47 ± 0.04
Diameters of C and Sc (mm)	1.12	Young's modulus of vein (MPa)	0.65 ± 0.06
Diameters of other veins (mm)	1.02	Young's modulus of membrane (MPa)	0.30 ± 0.01
Membrane thickness (mm)	0.5	Poisson's ratio υ	0.25

The wing veins belong to composite elastic materials, and their material mechanical properties were measured by the nanoindentation testing system in our previous work [38]. The calculation equation between the reduced modulus *E*r (obtained from the test) and Young's modulus *E* is as follows [40]:

$$\frac{1}{E_r} = \frac{1 - v^2}{E} + \frac{1 - v_i^2}{E_i} \tag{1}$$

The veins were divided into tiny continuous units in the form of continuous variables density function. The density of each element was used as the design variable, and the relative density (x^p) was defined within the range of [0, 1] to find the main loading force transmission path. The topology optimization of the veins was transformed into the optimal distribution of the material for the vein continuous unit,

$$p = x^p p_1 \tag{2}$$

where ρ_1 and ρ are the initial material density of each element and that after topology optimization, respectively. When x^p within the range of [0, 1], the interpolation function was introduced to calculate Young's modulus *E.* The relationship between x^p and *E* was established. The minimum compliance method (SIMP) is used [32],

$$E_i = E_{min} + x_i^p(E_0 - E_{min}), i \ = 1, 2, \dots, N \tag{3}$$

where E_i, E_0 , and E_{min} represent the interpolation modulus, the initial Young's modulus of unit *i* and the Young's modulus of hole, respectively. *N* is the number of finite elements, and *p* is the penalty factor. In the process of topology optimization, the volume of wing veins was set as the objective function. Stress and static displacement under uniform load were set as the constraint conditions. The objective function of topology optimization can be expressed as:

$$V_0 = \sum_{i=1}^{N} V_i x_i^p, i = 1, 2, \dots, N \tag{4}$$

$$X = \left[x_1^p, x_2^p, \dots, x_i^p\right], i = 1, 2, \dots, N \tag{5}$$

where ***X*** is the vector of design variables, V_O is the total volume of wing veins, and V_i is the volume of wing unit. The optimization of the objective function is constrained by the following parameters,

$$D_l < [D] \tag{6}$$

$$\xi_i = \sqrt{\xi_x^2 + \xi_y^2 - \xi_x \xi_y + 3\gamma_{xy}^2} \leq [\xi_b] \tag{7}$$

where D_l is the static displacement of the hindwing model in the direction of load, and [*D*] is the limit of D_l, which obtained from the structural mechanics analysis. ξ_i is the element stress, [ξ_b] is the ultimate strength of veins.

2.2 Mechanical Characteristics of the Flexible Wing Model and FWMAV Flapping Mechanism

2.2.1 Flexible Wing Model and Mechanical Characteristics Analysis

To explore the best design of the flexible wing skeleton, the simple model (Fig. 3a, Pro-model), the bionic wing vein model (Fig. 3b, Bio-model), and the obtained topology optimization analysis model (Fig. 3c, Top model) were used as the control group. The structural mechanics and vibration modal characteristics were compared and analyzed.

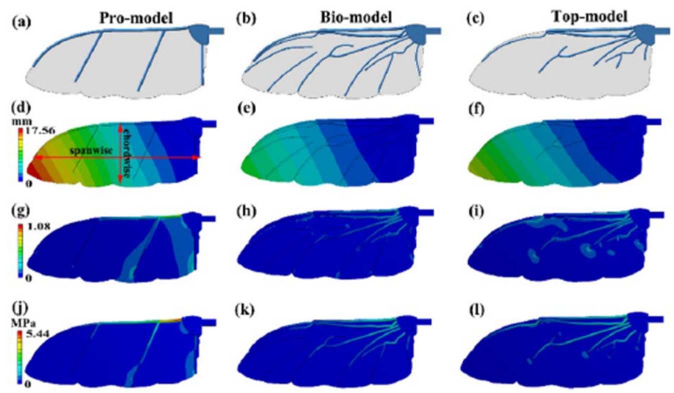

Figure 3 Structural design and mechanical characteristics of bionic wing models.

The airfoil data of the three models were the same (using the hindwing airfoil data of *T. dichotomus*). Combined with the actual situation of 3D printing, a polyamide elastic film was used as the wing membrane material. SLA photo-curable resin was used as the wing skeleton material. The linkage unit was made of the same material as the wing skeleton. Material properties of the bionic wing model are present in Table 2.

Table 2 Material properties of the bionic wing model.

Parameters	Density (g/cm^3)	Young's modulus MPa	Poisson's ratio
Wing skeleton	1.1	200	0.25
Wing membrane	1.15	700	0.25
Linkage unit	1.1	200	0.25

In ANSYS Workbench, to analyze the structural mechanical and mode properties of bionic wing models, the model was first divided into three bodies: the connecting element, the skeleton, and the wing membrane. The material properties of each element were assigned to the model. Because the size of each element is different, the mesh was divided. The size of the mesh element was 0.5 mm. Because the structure of the model was not complicated, automatic mesh division was used to divide the model. The number of grid components after partitioning was 202,507 nodes and 67,962 elements for Promodel, 213,902 nodes and 73,365 elements for Bio-model, and 203,710 nodes and 67,937 elements for Top model. The element quality and skewness of the three models were sufficient to meet the needs of structural mechanic analysis.

In order to simulate the supporting role of the bionic wing model in the hover flight, the model connecting elements were applied to fixed constraints, and uniform load Q was applied to the surface of bionic wing model,

$$\begin{cases} F = mg = 7.47 \times 10^{-2} N \\ Q = \dfrac{F}{2A} = 4.4 \times 10^{-5} MPa \end{cases} \tag{8}$$

where *F* is hovering wing lift, *Q* is uniform load. In ANSYS, the bionic wing element entities were discretized into a finite number of system, for arbitrary element (*e*), point displacement (***l***) , strain (***ε***), and stress (***σ***) are,

$$\begin{cases} [l] = [u, v, w] \\ [\varepsilon] = \left[\varepsilon_{xx}, \varepsilon_{yy}, \varepsilon_{zz}, \varepsilon_{xy}, \varepsilon_{yz}, \varepsilon_{zx}\right] \\ [\sigma] = \left[\sigma_{xx}, \sigma_{yy}, \sigma_{zz}, \sigma_{xy}, \sigma_{yz}, \sigma_{zx}\right] \end{cases} \tag{9}$$

According to the theory of elastic material, ***ε*** and ***l*** should satisfy the geometric relationship,

$$[\boldsymbol{\varepsilon}] = [L][l] \tag{10}$$

where [***L***] is the differential operator 3D matrix. The σ and ε of bionic wing should satisfy:

$$[\sigma] = [D][\varepsilon] \tag{11}$$

where [***D***] is 3D elastic matrix. Applying the principle of virtual work to the volume of arbitrary element of the bionic wing model, can obtain ***l*** at any point, through the point displacement and interpolation function [41]. Then the relationship between ε and the point displacement vector ([$\boldsymbol{u}^e$]) is as follows:

$$[\varepsilon] = [L][N][u^e] \tag{12}$$

wing structure requires two basic conditions: the balance of node; the degrees of freedom between adjacent units on node are coordination. Therefore, the stiffness of adjacent elements on common node is superimposed together to resist the displacement forming the overall structural equation,

$$\sum_e [K^e][U] = \sum_e \left[F^{ef}\right] + \sum_e [F^{eS}] + \sum_e [F^{eC}] \tag{13}$$

where [***U***] is structural node displacement vector, [$\boldsymbol{K}^e$] is node stiffness matrix, [$\boldsymbol{F}^{ef}$], [$\boldsymbol{F}^{eS}$] are volume force, surface force equivalent node vector, respectively. [$\boldsymbol{F}^{eC}$] is the element node concentrates load vector.

In order to simulate the dynamic stability of the bionic wing model, mode analysis was used to determine the natural frequency and mode of vibration so as to avoid the bionic wing resonance under the flutter frequency which will cause damage. The theoretical dynamic equation of bionic wing vibration is

$$[M]\{\dot{x}_i(t)\} + [C]\{\ddot{x}_i(t)\} + [K]\{x_i(t)\} = \{F(t)\}$$
(14)

is element damping matrix, [***K***] is element stiffness matrix, $\dot{x}_i(t)$ is element velocity, $\ddot{x}_i(t)$ is element acceleration, and $x_i(t)$ is element displacement. While for the bionic wing model, it does not involve damping factors, only considers its mass and stiffness factors. Thus, the equation can be obtained:

$$[M]\{x\dot{x}_i(t)\} + [K]\{x_i(t)\} = 0$$
(15)

Its characteristic equation is as follows:

$$|[K] - \omega^2[M]| = 0$$
(16)

Thus, the natural frequency is calculated

$$f = \frac{\omega}{2\pi}$$
(17)

2.2.2 FWMAV Flapping Mechanism

Figure 4 shows the transmission mechanism of the FWMAV, composed of a pedestal, moto gear, linkage rod, 1st-stage gear, 2nd-stage gear, and pendulum rod, made of resin as the base material substrate by 3D printing. A miniature DC motor (BETAFPV, 716MD, China) is selected as the driving source. The motor specification is 7 mm × 16 mm × 0.8 mm, the output shaft length is 0.8 mm, the rated voltage is 3.4 V, the starting voltage is 0.5 V, the rated current is 80 mA, and the maximum speed is 70000 r/min. After the assembly, the maximum flapping frequency of the FWMAV prototype is 14 Hz.

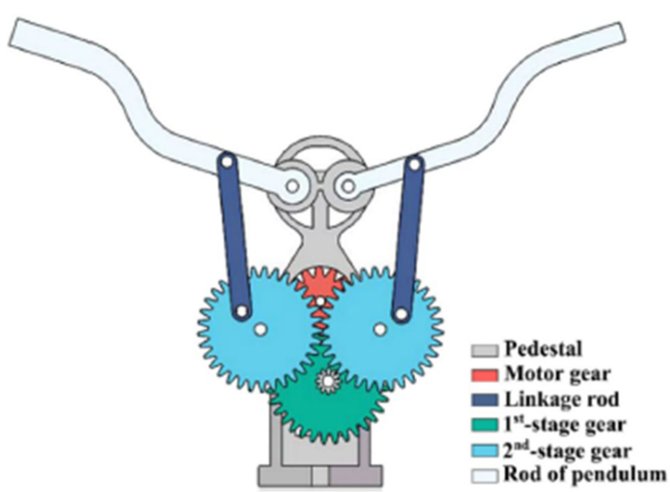

Figure 4 FWMAV flapping mechanical device.

2.3 Flexible Wing 3D Printing Design and Analysis of the FWMAV Vibration Characteristics

2.3.1 Flexible Wing 3D Printing Design and Mass Determination

Due to the irregular shape and small size of the skeleton of the models, 3D printing is the most reasonable method for their manufacture. The selection of skeleton material should follow the principle of being convenient for 3D printing, exhibiting high hardness and low density. Therefore, SLA light-curing 3D printing resin was selected as the skeleton material. Wing membrane materials should be selected with good elasticity, high fatigue strength, low density, and ease of cutting. Polyamide elastic film and machine-made paper were selected.

The three models and two wing membranes were bonded together with adhesive (Fig. 5). Membrane I and membrane II are bionic wing membranes made of machine-made paper and polyamide elastic film, respectively.

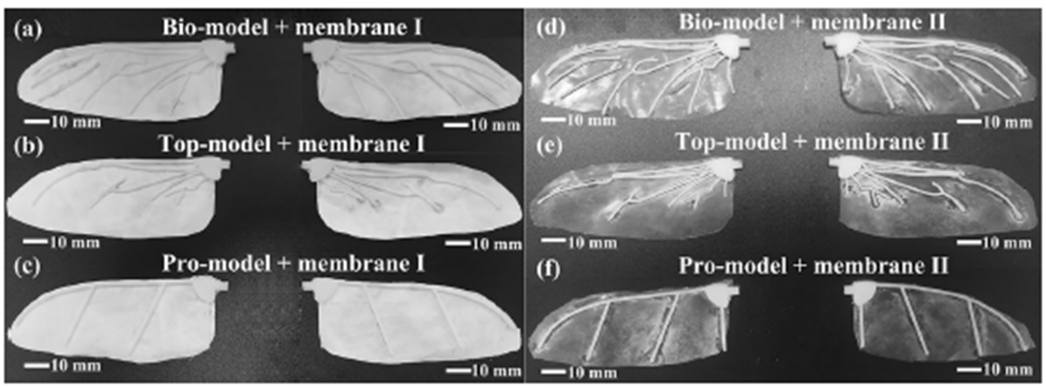

Figure 5 Flexible wing 3D printing design.

2.3.2 Analysis of the FWMAV Vibration Characteristics

Six kinds of bionic wings were connected to the FWMAV and tested in a low-speed DC wind tunnel (Fig. 6). The airflow enters the working section from the rectifying section through the inlet. The triaxial force transducer (LH-SZ-02, LH, China) can detect the real-time fluctuation of the force in the X–Y–Z direction, which is the force vibration direction of the FWMAV when flapping. The sampling frequency of the triaxial force transducer is 500 Hz, and the sampling time is 10 s. The collected force signal is de-noised by the wavelet de-noising method [42, 43].

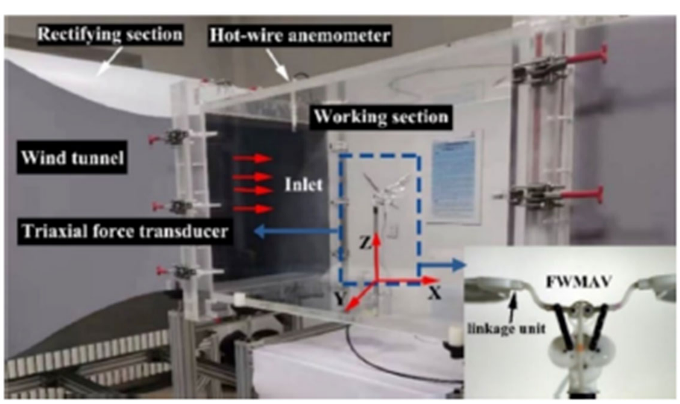

Figure 6 Wind tunnel and the triaxial force transducer.

Limited by the material and equipment level of the flapping wing mechanism, when the flapping frequency of the bionic wing is higher than 12 Hz, the vibration of the transmission mechanism is large, and long-term stable operation is difficult. Therefore, three frequency gradients (8 Hz, 10 Hz, and 12 Hz) with flapping frequencies lower than 12 Hz are selected as the experimental group. For the flapping mechanical device vibration characteristics under aerodynamic force, the rectification section of the wind tunnel was removed, and a high-speed digital camera (Phantom V711, Vision Research, Wayne, NJ, USA) was placed immediately in front of the device to observe the flapping situation and record the force data in real time.

In the FWMAV wind tunnel test, it was found that when the wind speed exceeded 3 m/s, the wings of the FWMAV were susceptible to the influence of the wind speed and greatly affected. In a previous study by our research group, it was also found that the average lift generated by the wings decreased significantly when the wind speed exceeded 3 m/s. Therefore, this study used three different wind speed gradients with wind speeds lower than 3 m/s as the experimental group to study the wind resistance performance of the FWMAV.

$$R_e = \frac{\rho \upsilon d}{\mu} = \frac{\theta_{min} f L^2}{\mu \lambda a} \tag{18}$$

ρ, the fluid density under the normal temperature air density, is 1.293 kg/m^3; *v* is the fluid velocity of 1 m/s, 2 m/s, and 3 m/s; *d* is the characteristic length (string length, 4 cm); μ is the viscosity for air movement, and at room temperature, the value is 1.789 × 10^{-5} kg/(m s); θ*max* is the amplitude of the flapping angle (approximately 75°); *f* is the flapping frequency of 8 Hz, 10 Hz, and 12 Hz; L is the wingspan (9 cm); and λ*a* is the aspect ratio (2.25). Upon substituting the above parameters into the Reynolds number calculation formula, the Reynolds numbers at different wind speeds and frequencies are 2.891 × 103, 5.782 × 103, 8.673 × 103, 1.49 × 103, 1.86 × 103, and 2.24 × 103.

The Strouhal Number $S = \omega L/v$, where ω is the circular frequency ($2\pi f$), *L* is the length of the wingspan, and *v* is the wind speed. The Strouhal Numbers are 2.26, 2.87 and 3.39 when the fixed wind speed is 2 m/s and flutter frequency is 8 Hz, 10 Hz, and 12 Hz, respectively. When the fixed frequency is 12 Hz and the wind speed of the test section is 1 m/s, 2 m/s, and 3 m/s, the Strouhal Numbers are 6.78, 3.39, and 2.26, respectively.

3 Results and Discussion

3.1 Hindwing Model Topology Optimization Analysis

The results of the topology optimization analysis of the wing veins of the hindwing model indicated that the most sensitive part of the mass response (red area in Fig. 2c) was mainly concentrated in the end piece of the costa vein (C) and the subcostal vein (Sc), the anal vein (1A, 2A, 3A), the end piece of the radius branch vein (R1 and R2), the middle and end piece of the media vein (M), the cubitus branch vein (Cu1 and Cu2), and the end piece of the jugal vein (J). This indicates that the above vein unit is not the main force transmission path of the hindwing. Removing some of its mass will not have a great influence on the structural and mechanical properties of the hindwing model. The gray area in Fig. 2c is the wing vein unit whose mass should be preserved after calculation, namely the main force transmission path of the hindwing vein model.

Based on the calculation results and replacing the hindwing base with the linkage unit that can connect with the FWMAV body, the topology optimization model of the hindwing veins is shown in Fig. 2d.

In this model, considering the coherence and realizability of 3D printing, the costa vein (C), the subcostal vein (Sc), and the anal vein (1A) were retained as a whole, and the anal vein (2A), the anal vein (3A), and the red parts of the remaining vein units were removed.

3.2 Mechanical Characteristics of the Flexible Wing Model and the FWMAV Flapping Mechanism

3.2.1 Structural Mechanical Characteristics

As shown in Fig. 3d, e and f, the overall displacement and deformation trends of the three models are similar. The difference is that Pro-model has the displacement deformation located at a relatively forward position in the span-wise direction, while Bio-model and Top model have the displacement deformation located at a relatively aft position. This indicates that the flexible wing model based on beetle hindwings has a stronger ability to resist displacement deformation in the span-wise direction. The maximum displacement shape variables of the models are 17.56 mm, 8.48 mm and 11.90 mm, which occur in the tail. This indicates that the skeleton structure of the models can resist the uniformly distributed load better, but the effect for Bio-model and Top model is more obvious. Because the number of vein units was reduced, the load-resisting effect of Top model is slightly decreased compared with that of Bio-model.

As shown in Fig. 3g, h and i, the maximum strain of Promodel is 0.68, which occurs at the crosswise skeleton close to the linkage unit. Along the span-wise direction of the first two longitudinal skeletons, the strain distribution is concentrated. The maximum strain of Bio-model is 1.08, but no concentrated strain distribution is observed. The location of the maximum strain is not obvious, and near the skeleton and the linkage unit, a strain distribution of 0.15–0.38 is generated. The maximum strain of Top model is 0.86, which is smaller than that of Bio-model but larger than that of Pro-model. The results indicate that Bio-model has the strongest overall strain resistance, but the maximum strain that occurred is the largest. The strain resistance of Promodel is the weakest, and the elastic strain concentration is in the largest range. The ability of Top model to resist strain occurrence is moderate, and the strain distribution range is minimal.

As shown in Fig. 3j, k and l, the maximum stress of Promodel is 5.44 MPa, concentrated in the skeleton close to the linkage unit. The maximum stresses of Bio-model and Top model are 2.81 MPa and 2.76 MPa, respectively. However, the stress of most skeleton groups is concentrated in the range of 0.40–1.00 MPa, without a large range of stress concentration distributions. The results show that the stress resistance of Top model and Bio-model is better than that of Pro-model, and the structural mechanical properties of the two models are similar.

It can be inferred that all the models have a good ability to resist displacement and deformation, but the elastic strain–stress characteristics are different. Pro-model tends to develop a large range of strain–strain concentrations with poorer structural mechanical properties and loading capacity. The stress–strain characteristics of Top model and Biomodel are similar, and there is no concentration over a wide range. This result indicates that Top model and Bio-model have better structural and mechanical properties and are more suitable for use as the carrier frame of the FWMAV.

3.2.2 Vibration Mode Characteristics

Figure 7a–f shows the vibration mode characteristics of Promodel. The natural frequency of the first mode is 1.36 Hz, and the mode shape shows an “up-down flapping” mode along the span-wise direction, and the largest deformation occurs at the tail of the model. The natural frequency of the second mode is 4.88 Hz, and the mode shape shows an “upward torsional” mode along the chordal direction in the middle of the model, resulting in the largest deformation. The third natural frequency is 7.90 Hz; the middle of the model bends downward, and the tail twists upward. The fourth and fifth natural frequencies are 10.23 Hz and 16.45 Hz, respectively. The model is curved in the spanwise direction and twisted chordwise. However, the bending directions are opposite to each other, and the torsion directions are similar. The natural frequency of the sixth mode is 19.39 Hz and does not have regular bending and torsion characteristics on the whole. It can be inferred that when the vibration frequency of Pro-model is lower than 7.90 Hz, the single deformation of torsion or bending is more likely to happen. The frequency of bending deformation is lower, while the frequency of torsional deformation is higher. When the vibration frequency is between 7.90 Hz and 16.95 Hz, Pro-model is susceptible to deformation resulting from a combination of torsion and bending. When the vibration frequency exceeds 19.39 Hz, the vibration deformation around Pro-model is large, and it no longer exhibits good modal vibration mechanical behavior.

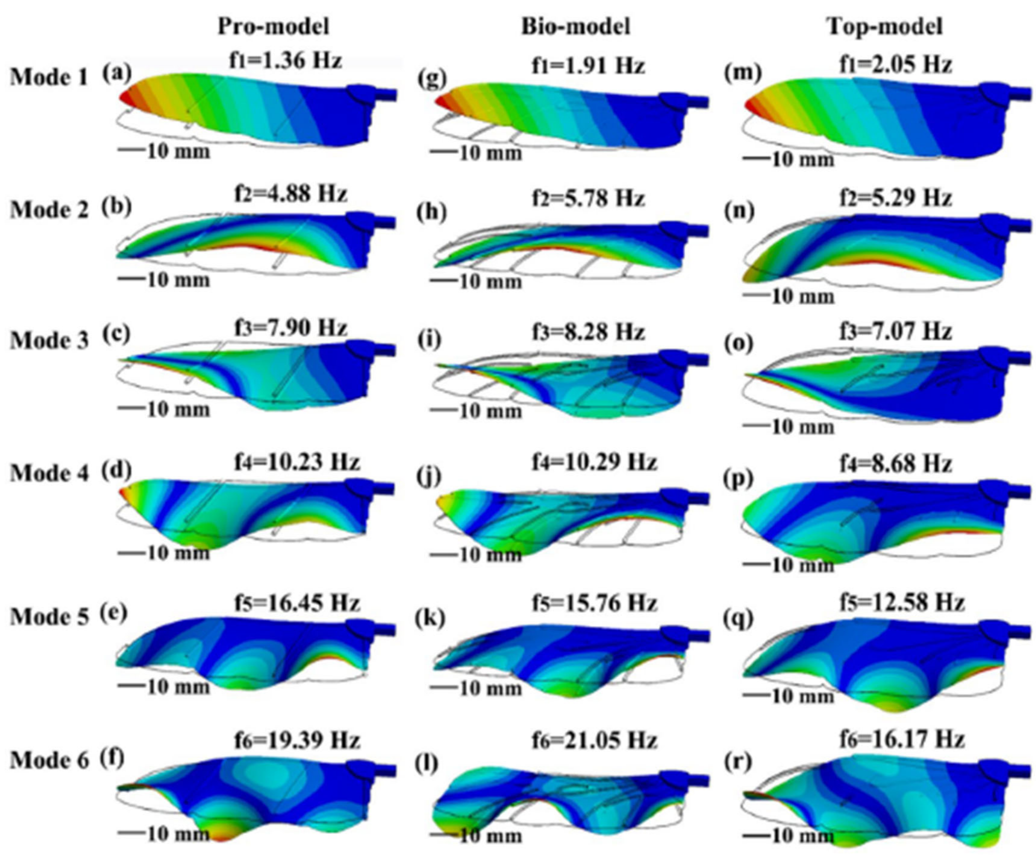

Figure 7 Vibration mode characteristics.

Figure 7g–l shows the vibration mode characteristics of Bio-model. The bending and torsional deformation regulations of Bio-model and Pro-model are similar. Both show single bending and torsional deformation at the first three natural frequencies, with combined bending and torsional deformation at the fourth and fifth natural frequencies, and both lose regular deformation characteristics at the sixth natural frequency. However, the natural frequencies of Biomodel are slightly higher than those of Pro-model, and the vibration deformation amplitude is slightly smaller. When the vibration frequency is higher than 21.05 Hz, the deformation around Bio-model is larger, the original characteristic shape is lost, and the regular bending and torsional deformation regulations are no longer available. It can be inferred that compared with Pro-model, the skeleton of Bio-model has stronger support for the wing membrane and has better dynamic stability, which is conducive to flapping at higher frequencies and obtaining higher lift forces.

Figure 7m–r shows the vibration mode characteristics of Top model. The bending and torsional deformation regulation of Top model is similar to that of the other models. However, the natural frequency without airfoil characteristics is the lowest, and the maximum vibration amplitude is the smallest. This is because the airfoil and material of the models are the same, and the change regulations of the overall displacement deformation are similar. When vibrations occur at different frequencies, the deformation regulations are similar. In addition, due to the different distributions and combinations of skeleton elements, the vibration frequency and amplitude are different.

3.2.3 FWMAV Flapping Mechanism Characteristics

As shown in Fig. 8a–c, it is found by imaging with the highspeed digital camera that when the transmission mechanism of the FWMAV drives the two wings to rotate up, the linkage mechanism suddenly “stops” (dead point) when it reaches the highest position. At this time, due to the sudden stagnation of the linkage mechanism, the 2nd-stage reduction gear changes from downward meshing rotation to upward meshing rotation, and the rod of the pendulum swings to the highest point and slowly falls back due to the combined action of inertia and gravity.

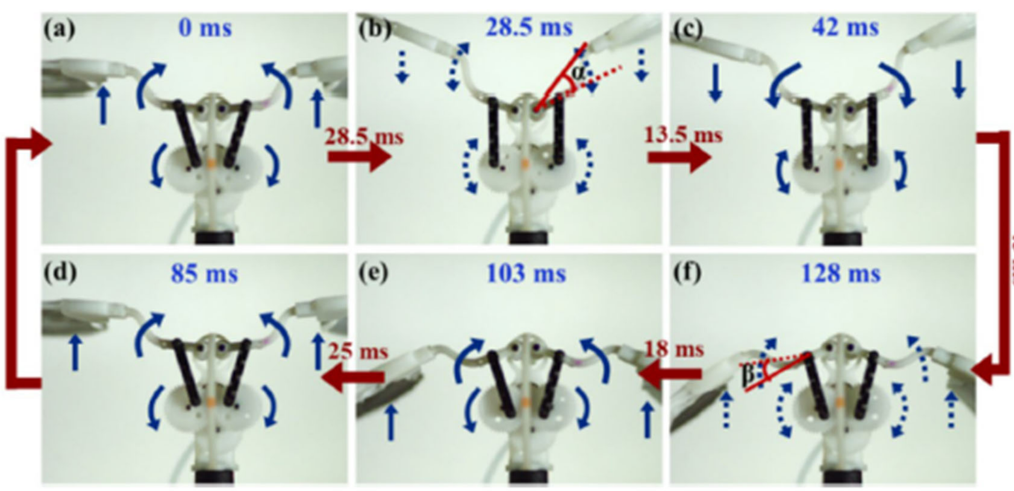

Figure 8 Flapping process of the FWMAV when the flapping frequency is 8Hz.

As shown in Fig. 8d, e, the 2nd-stage reduction gear continues to rotate downward under the engagement of the 1st-stage gear, and the rod of the pendulum starts to move downward from the highest position and accelerates to swing downward. When the linkage rod moves to the lowest position, the mechanism suddenly “stops” again. The 2nd-stage reduction gear undergoes motion mutation, and the rod of the pendulum moves to the lowest position and stops under the action of inertial forces and gravity. As the 1st-stage gear continues to rotate, the linkage rod moves upward from the lowest point and drives the rod of the pendulum upward, and the wings rise to the starting position to complete a flapping cycle.

The results show that when the rod of the pendulum swings upward to the top and downward to the bottom, the 2nd-stage reduction gear undergoes "rotational mutation", the rod of the pendulum experiences "rotation stagnation", and the "reciprocating angle" also appears, named α and β. This is also the prime reason for the vibration of the FWMAV. When the flapping frequency is 8 Hz, the downflapping stroke time is 43 ms, the downward "rotation stagnation" time is 18 ms, the up-flapping stroke time is 53.5 ms, the upward "rotation stagnation" time is 13.5 ms, the ratio of up and down stroke time is 1.24, and the ratio of "rotation stagnation" time is 0.75.

3.3 Flexible Wing 3D Printing Design and FWMAV Vibration Characteristics Analysis

3.3.1 Flexible Wing 3D Printing Design and Mass Determination

The mass determination (Fig. 9) of the three models after 3D printing shows that the skeleton weight of Bio-model is 0.92 ± 0.08 g and that of Top model is 0.78 ± 0.06 g. This shows that the mass of the skeleton model can be reduced by 15.22% after topology optimization analysis. The results prove that topology optimization analysis can effectively reduce the mass of the bionic wing while maintaining the mechanical properties of the model structure. After assembling three kinds of skeleton structures and two kinds of wing membranes, it is found that the mass of the same model with membrane II is smaller than that with membrane I.

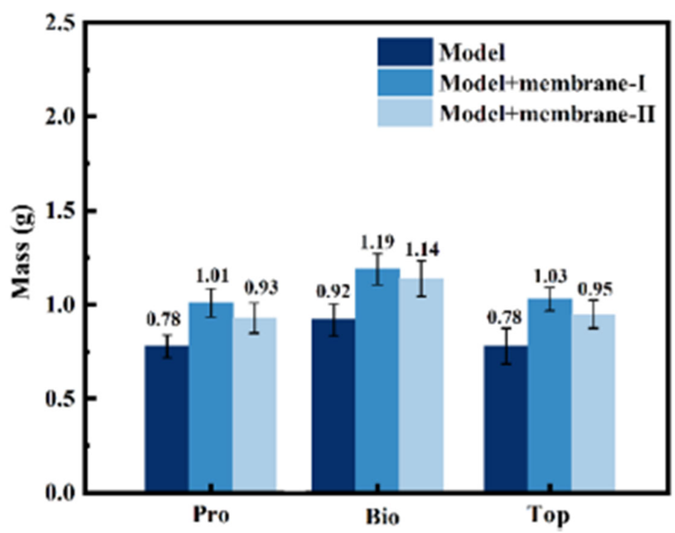

Figure 9 Flexible wing mass determination.

3.3.2 Vibration Characteristics at Different Flapping Frequencies

Figure 10 shows the force amplitude time domain diagram of the models at different flapping frequencies with a fixed wind speed of 2 m/s. Figure 10a, d, b, e, c and f shows the force fluctuation of Pro-model in the X-, Y-, and Z-axis directions, respectively. The figure shows that when the FWMAV flaps at frequencies of 8 Hz, 10 Hz, and 12 Hz, the force fluctuation in the X-axis and Y-axis obviously increases with increasing flapping frequency. The wave peaks are more pronounced, and the waveform is sharper and has no obvious periodic characteristics. The results show that the vibration amplitude in the front and back and left and right directions is greatly affected by the flapping frequency. The dynamic instability characteristics are significant, and under the comprehensive influence of the inertial force and aerodynamic force, the impact effect is obvious. When the flapping frequency reached 12 Hz, more high and sharp peak fluctuations appeared in the X-axis direction, but the peak fluctuations of membrane II are significantly less than those of membrane I. These results indicate that when Pro-model is used as the skeleton and flapping model at a higher frequency, the vibration amplitude is larger and the dynamic stability poor. Because of the lighter weight and stronger elasticity, the impact resistance of membrane II is better than that of membrane I.

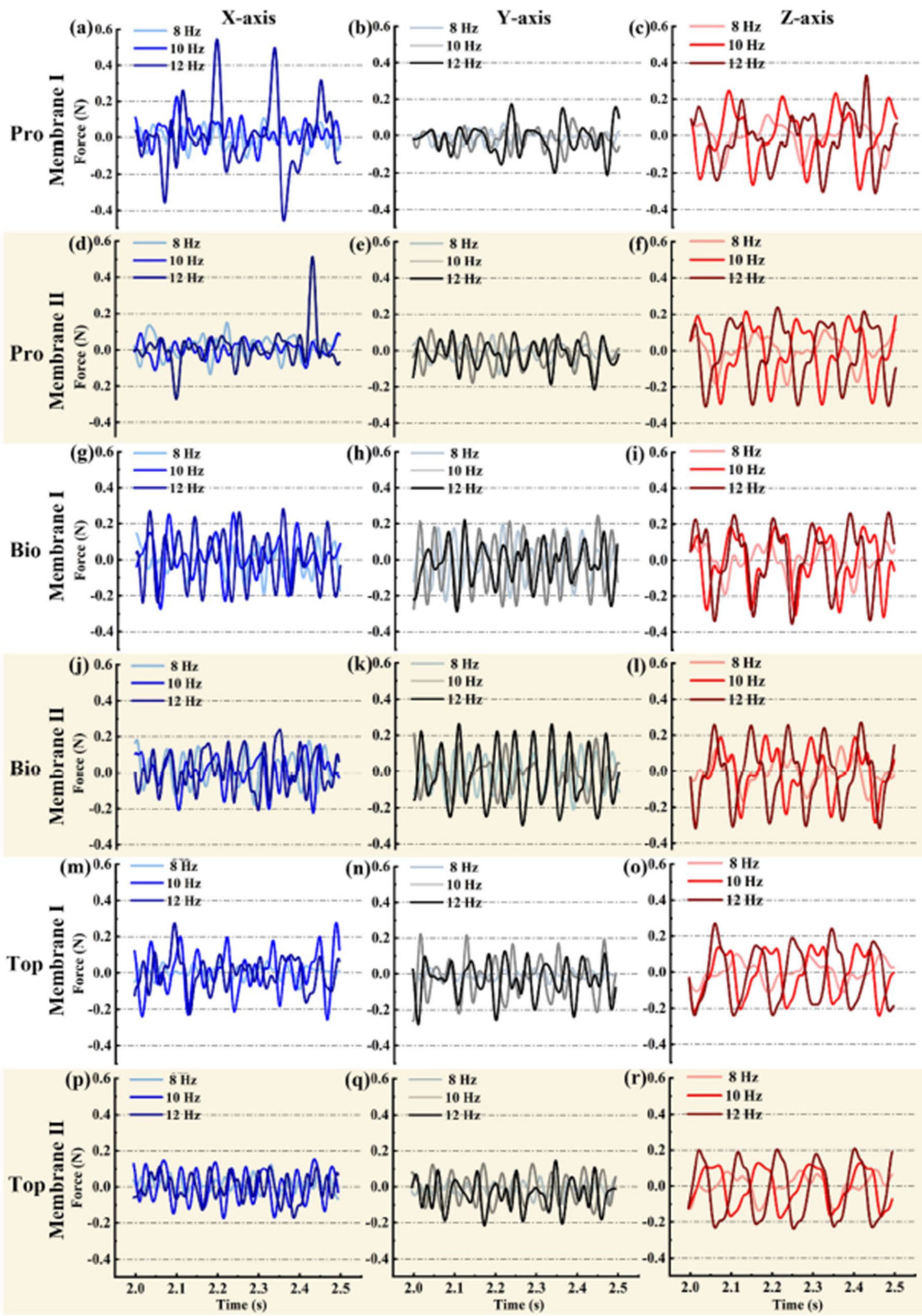

Figure 10 Vibration characteristics of the three kinds of models at different flapping frequences.

The force fluctuation has obvious periodic harmonic vibration characteristics in the Z-axis direction. The initial phase of flapping at different frequencies is the same, but at 10 Hz and 12 Hz, the peak shifts to the left, and the number of periods is positively correlated with the flapping frequency. Over one flapping cycle, there are two unilateral shaving phenomena at the positive peak in the Z-axis direction at three kinds of frequencies. This is mainly because in the flapping process of the FWMAV, the flapping mechanism appears at twice the “dead point”, and wing flapping occurs at twice the “stagnation”, which hinders its ability to obtain lift. At 8 Hz, the peak shaving phenomenon is the most significant, but the waveform amplitude is the smallest, and the amplitude stability is the best. At 12 Hz, the amplitude of the waveform is the largest, the membrane I waveform has more higher harmonics, and the roughness is stronger. According to the overall stress in the Z-axis direction, for membrane II compared with membrane I, the waveforms are more stable at the three frequencies. In addition, the case of higher harmonics occurs less frequently, the shaving phenomenon of the positive peak is not obvious, and the vibration resistance is better.

As shown in Fig. 10g, j, h, k, i and l, compared with Pro-model, when Bio-model is the skeleton, the peak height and waveform roughness of the force fluctuation in the X-axis direction are greatly decreased. This shows that the dynamic stability of Bio-model is better than that of Pro-model in the X-axis direction. This is due to the better support of the Bio-model wing membrane with relatively low deformation. When the flapping frequency is 8–10 Hz, the mode vibration deformation of Bio-model is small, and the resistance to external force impact is strong. The double peak amplitude of the force on the Y-axis is higher. This is because the mass of Bio-model is higher than that of Pro-model. Under the influence of inertial forces, when the wings are flapping, they create more influence on the X- and Y-axes, and the amplitude of vibration under force is large. However, in the Z-axis direction, the Bio-model amplitude stability of the stress waveform is better, no obvious higher harmonics are found in the two peaks, and the shaving phenomenon of the positive peak is obviously reduced. The results show that the anti-vibration performance of Bio-model is better than that of Pro-model. When Bio-model is used as the skeleton, the number of wave peaks on the X-axis and Y-axis of membrane II is less than that of membrane I, and the degree of waveform roughness is lower. This proves that the vibration resistance of membrane II is still better than that of membrane I.

As shown in Fig. 10m, p, n, q, o and r, compared with the former models, the stress waveform of Top model on the X-axis and Y-axis is significantly less than that of Promodel, and the amplitude of the peaks is lower than that of Bio-model. This is because the mechanical properties and structural support ability of Top model are better than those of Pro-model, and the modal vibration amplitude is lower, so the dynamic stability is better. After topology optimization analysis, the structural mechanical properties of Top model are close to those of Bio-model, but the mass is lower. Therefore, the inertial force has little effect on the flapping of the wings, and the amplitude of the force vibration is lower. Compared with the Bio-model results, the force waveform on the Z-axis and the positive peak shaving phenomenon of Top model are lower. When the flapping frequency is 12 Hz, positive peak shaving is almost eliminated, indicating that Top model has a more stable ability to gain lift.

3.3.3 Vibration Characteristics at Different Wind Speeds

Figure 11 shows the force amplitude time domain diagram of the two kinds of wing membrane materials at different wind speeds with a fixed flapping frequency of 12 Hz while the three models are used as the skeleton. Compared with Fig. 10, the force vibration amplitude of Pro-model in the X-axis under the three wind speeds is higher. The overall shaking degree of the FWMAV is the strongest when the wind speed is 1 m/s, followed by 3 m/s, and the smallest result occurs when the wind speed is 2 m/s. This is because the wind speed direction is parallel to the X-axis direction. When the wind speed is at its minimum (1 m/s), the wings flap vigorously, and the wind generates positive excitation on the vibration, so the fluctuation degree is the largest. When the wind speed further increases (2 m/s), the wind force inhibits the flapping of wings in the X-axis direction, so the force fluctuation degree is the smallest. When the wind speed is 3 m/s, although the flutter of the wings is inhibited to a certain extent, the wind has a great effect on the whole FWMAV, so the force fluctuation degree is moderate.

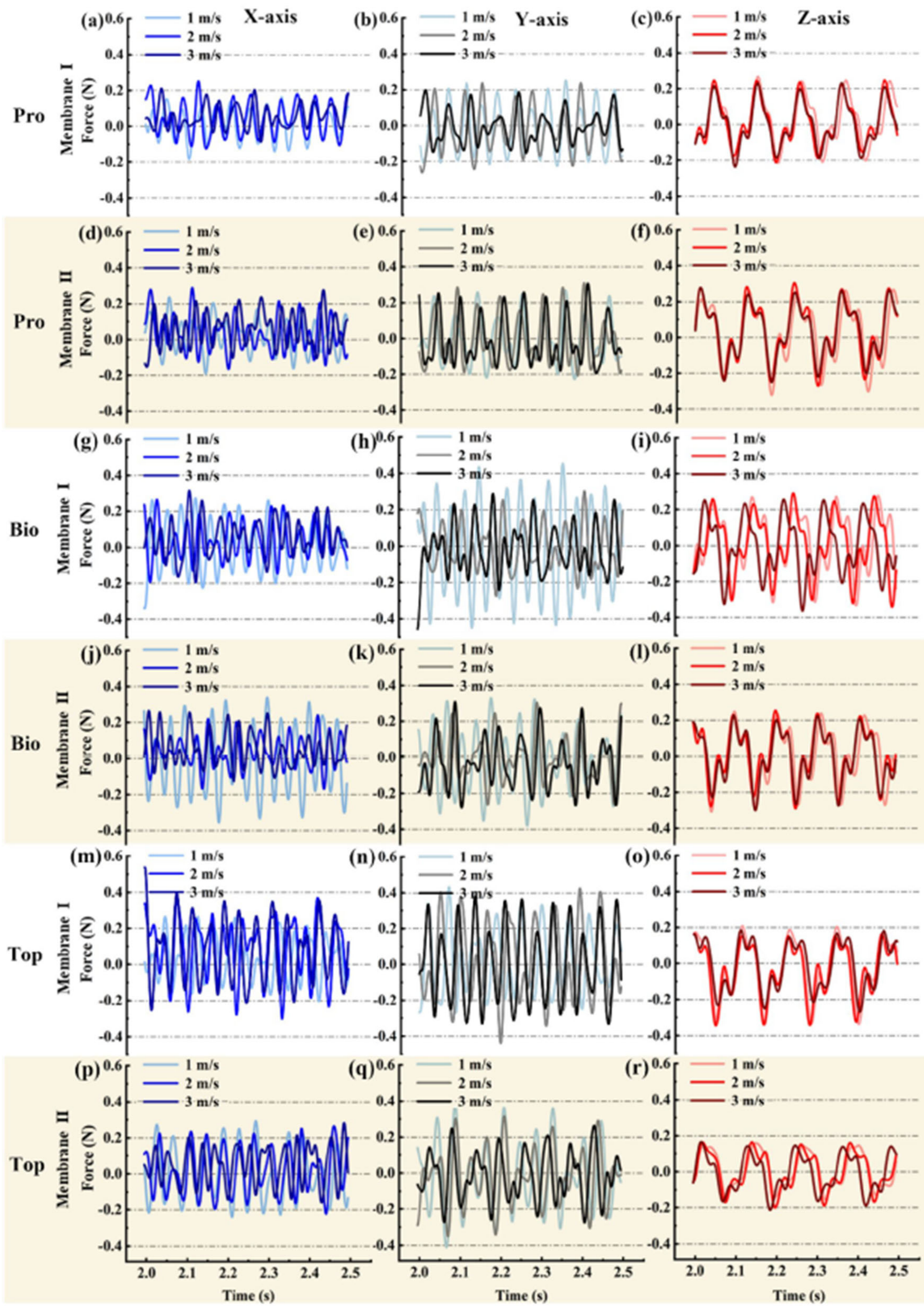

Figure 11 Vibration characteristics of the three kinds of models at different wind speeds.

The force vibration amplitude of Pro-model on the Y-axis is higher than that without wind. The overall shaking degree is the strongest when the wind speed is 1 m/s, followed by 2 m/s, and the smallest occurs when the wind speed is 3 m/s. This is because the wind is perpendicular to the Y-axis, restraining the flapping of the wings and reducing the amplitude, but the wind does not exert a force on the Y-axis. Since the angle of attack is not set, the wind speed direction is perpendicular to the Z-axis direction, and the force on the Z-axis mainly comes from the flapping of the wings; therefore, the force fluctuation curves of the wind speeds coincide with the fluctuation curves of Fig. 10 when the flapping frequency is 10 Hz. The force fluctuation degree of membrane II on the X-axis and Y-axis is smaller than that of membrane I, which indicated that it has better wind fluctuation resistance.

As shown in Fig. 11, the force fluctuation amplitudes of Bio-model on the X- and Y-axes are significantly smaller than those of Pro-model; the number of wave peaks is much lower, and the amplitude stability is better. This is because the structural mechanical properties of Bio-model are better than those of Pro-model, and the resistance to deformation and wind is excellent.

As shown in Fig. 11, compared to the Bio-model and Pro-model results, the force fluctuation amplitudes of Top model on the X- and Y-axes are intermediate. This corresponds to the supporting ability of the three models on the wing membrane. However, with the combination of Top model and membrane II, the force fluctuation on the Z-axis is obviously better than that of Bio-model and Pro-model; the waveform curve is the smoothest, no obvious higher harmonics were observed, and only one shaving phenomenon occurs in the flapping cycle. This is because the combination of Top model and membrane II has a lower mass and minimum inertial force while maintaining a certain supporting capacity. This demonstrates that the combination of Top model and membrane II produces the best dynamic stability.

4 Conclusions

This paper determined the main force transmission path of the hindwing by topology optimization analysis and the Top model was established. Compared with bionic wing model Bio and classical wing model Pro, Top has better structural mechanical characteristics and dynamic stability. SLA light-curing resin was selected as the skeleton material, machine paper (membrane I) and polyamide elastic film (membrane II) were selected as the wing surface materials to manufacture FWMAV. When the FWMAV flapped, the 2nd-stage reduction gear will exhibit the “rotational mutation” phenomenon, and the linkage will suddenly experience “stagnation” twice. This was the main reason for the vibration of the FWMAV. Wind tunnel and force sensor were used to analyze the vibration characteristics of FWMAV with flexible wing under different aerodynamic parameters. When the Top model was used as the skeleton and polyamide elastic film (membrane II) was selected as the wing surface, the force amplitude was more stable, the roughness of the waveform and the peak shaving phenomenon of the Z-axis were the lowest, the actual dynamic stability was better. Of the model combinations tested, this combination was concluded to be the most suitable as a manufacturing solution for FWMAV wings.

Acknowledgements This work was supported by the National Natural Science Foundation of China (grant number 31970454), the Aviation Science Foundation of China (2020Z0740R4001), the Graduate Innovation Fund of Jilin University (2022189) and Undergraduate Innovation and Entrepreneurship Training Program Project of Jilin University (S202210183259).

Data Availability Data sharing is not applicable to this article as no datasets were generated or analyzed during the current study.

Declarations

Conflict of Interest The authors declare that there are no conflicts of interest regarding the publication of this article.

References

1. Nguyen, A. T., & Han, J. H. (2018). Wing flexibility effects on the flight performance of an insect-like flapping-wing micro-air vehicle. *Aerospace Science and Technology, 79*, 468–481. https://doi.org/10.1016/j.ast.2018.06.007
2. Muhammad, A., Nguyen, Q. V., Park, H. C., Hwang, D., Byun, D., & Goo, N. (2010). Improvement of artificial foldable wing models by mimicking the unfolding/folding mechanism of a beetle hind wing. *Journal of Bionic Engineering, 7*(2), 134–141. https://doi.org/10.1016/s1672-6529(09)60185-2
3. Phan, H. V., & Park, H. C. (2020). Mimicking nature's flyers: a review of insect-inspired flying robots. *Current Opinion in Insect Science, 42*, 70–75. https://doi.org/10.1016/j.cois.2020.09.008
4. Xiao, S. J., Hu, K., Huang, B. X., Deng, H. C., & Ding, X. L. (2021). A review of research on the mechanical design of hoverable flapping wing micro-air vehicles. *Journal of Bionic Engineering, 18*(6), 1235–1254. https://doi.org/10.1007/s42235-02l-00H8-
5. Hui, Z., Zhang, Y., & Chen, G. (2019). Aerodynamic performance investigation on a morphing unmanned aerial vehicle with bioinspired discrete wing structures. *Aerospace Science and Technology, 95*, 105419. https://doi.org/10.1016/j.ast.2019.105419
6. Wang, S. Q., Song, B. F., Chen, A., Fu, Q., & Cui, J. (2022). Modeling and flapping vibration suppression of a novel tailless flapping wing micro air vehicle. *Chinese Journal of Aeronautics, 35*(3), 309–328. https://doi.org/10.1016/j.cja.2021.08.030
7. Liu, H. (2020). Simulation-based insect-inspired flight systems. *Current Opinion in Insect Science, 42*, 105–109. https://doi.org/10.1016/j.cois.2020.10.001
8. Maxworthy, T. (1979). Experiments on the weis-fogh mechanism of lift generation by insects in hovering flight. Part 1. Dynamics of the 'fling.' *Journal of Fluid Mechanics, 93*(1), 47–63. https://doi.org/10.1017/S0022112079001774
9. Liu, H., Ellington, C., & Kawachi, K. (1998). A computational fluid dynamic study of hawkmoth hovering. *Journal of Experimental Biology, 201*(Pt4), 461–477. https://doi.org/10.1242/jeb.201.4.461
10. Wang, Z. J. (2000). Two dimensional mechanism for insect hovering. *Physical Review Letters, 85*(10), 2216–2219. https://doi.org/10.1103/PhysRevLett.85.2216
11. Wang, Z. J., Birch, J. M., & Dickinson, M. H. (2004). Unsteady forces and flows in low reynolds number hovering flight: two-dimensional computations vs robotic wing experiments. *The Journal of Experimental Biology, 207*(Pt 3), 449–460. https://doi.org/10.1242/jeb.00739
12. Aamer, S., Tian, F.-B., John, Y., & Joseph, L. C. S. (2016). Effects of wing shape, aspect ratio and deviation angle on aerodynamic performance of flapping wings in hover. *Physics of Fluids, 28*(11), 111901. https://doi.org/10.1063/1.4964928
13. Truong, T. V., Le, T. Q., Tran, H. T., Park, H. C., Yoon, K. J., & Byun, D. (2012). Flow visualization of rhinoceros beetle (*Trypoxylus Dichotomus*) in free flight. *Journal of Bionic Engineering, 9*(3), 304–314. https://doi.org/10.1016/S1672-6529(11)60127-3
14. Wang, L., Tian, F. B., & Lai, J. C. S. (2020). An immersed boundary method for fluid–structure–acoustics interactions involving large deformations and complex geometries. *Journal of Fluids and Structures, 95*, 102993. https://doi.org/10.1016/j.jfluidstructs.2020.102993
15. Krishna, S., Cho, M., Wehmann, H. N., Engels, T., & Lehmann, F. O. (2020). Wing design in flies: properties and aerodynamic function. *Insects, 11*(8), E466. https://doi.org/10.3390/insects11080466
16. Le, T. Q., Truong, T. V., Park, S. H., Truong, T. Q., Ko, J. H., Park, H. C., & Byun, D. (2013). Improvement of the aerodynamic performance by wing flexibility and elytra-hind wing interaction of a beetle during forward flight. *Journal of the Royal Society Interface, 10*(85), 20130312. https://doi.org/10.1098/rsif.2013.0312

17. Heathcote, S., Wang, Z., & Gursul, I. (2008). Effect of spanwise flexibility on flapping wing propulsion. *Journal of Fluids and Structures, 24*(2), 183–199. https://doi.org/10.1016/j.jfluidstructs.2007.08.003
18. Tercel, M. P. T. G., Veronesi, F., & Pope, T. W. (2018). Phylogenetic clustering of wingbeat frequency and flight-associated morphometrics across insect orders. *Physiological Entomology, 43*(2), 149–157. https://doi.org/10.1111/phen.12240
19. Wang, Y. J., Yin, Y. J., & Zheng, G. T. (2017). Fluid-coupled vibration control inspired by dragonfly wings. *Topics in Modal Analysis & Testing, 10*, 31–36. https://doi.org/10. 1007/978-3-319-54810-4_5
20. Combes, S. A., & Daniel, T. L. (2003). Into thin air: contributions of aerodynamic and inertial-elastic forces to wing bending in the hawkmoth manduca sexta. *The Journal of Experimental Biology, 206*(17), 2999–3006. https://doi.org/10.1242/jeb.00502
21. Rajabi, H., Rezasefat, M., Darvizeh, A., Dirks, J. H., Eshghi, S., Shafiei, A., Mostofi, T. M., & Gorb, S. N. (2016). A comparative study of the effects of constructional elements on the mechanical behaviour of dragonfly wings. *Applied Physics A, 122*(1), P19. https://doi.org/10.1007/s00339-015-9557-6
22. Wang, X. H., Zhang, Z. H., Ren, H. H., Chen, Y. L., & Wu, B. S. (2017). Role of soft matter in the sandwich vein of dragonfly wing in its configuration and aerodynamic behaviors. *Journal of Bionics Engineering, 14*(3), 557–566. https://doi.org/10.1016/S1672-6529(16)60421-3
23. Ha, N. S., Park, H. C., Goo, N. S., & Truong, Q. T. (2013). Relationship between wingbeat frequency and resonant frequency of the wing in insects. *Bioinspiration & Biomimetics, 8*(4), 046008. https://doi.org/10.1088/1748-3182/8/4/046008
24. Addo-Akoto, R., Ha, J.-S., & Han, J.-H. (2021). Roles of wing flexibility and kinematics in flapping wing aerodynamics. *Journal of Fluids and Structures, 104*, 103317. https://doi.org/10.1016/j.jfluidstructs.2021.103317
25. Wang, X. M., Zhou, W. Y., Xun, G. B., & Wu, Z. G. (2018). Dynamic shape control of piezocomposite-actuated morphing wings with vibration suppression. *Journal of Intelligent Material Systems and Structures, 29*(3), 358–370. https://doi.org/10.1177/1045389x17708039
26. Tsushima, N., & Su, W. H. (2017). Flutter suppression for highly flexible wings using passive and active piezoelectric effects. *Aerospace Science and Technology, 65*, 78–89. https://doi.org/10.1016/j.ast.2017.02.013
27. Tsushima, N., & Su, W. H. (2016). Modeling of highly flexible multifunctional wings for energy harvesting. *Journal of Aircraft, 53*(4), 1033–1044. https://doi.org/10.2514/1.C033496
28. Phan, H. V., & Park, H. C. (2020). Mechanisms of collision recovery in flying beetles and flapping-wing robots. *Science, 370*(6521), 1214–1219. https://doi.org/10.1126/science.abd3285
29. Akhter, M. Z., Ali, A. R., & Omar, F. K. (2022). Aerodynamics of a three-dimensional bionic morphing flap. *Sustainable Energy Technologies and Assessments, 52*, 102286. https://doi.org/10.1016/j.seta.2022.102286
30. Reid, H. D., Zhou, H. M., Maxcer, M., Peterson, R. K. D., Deng, J., & Jankauski, M. (2021). Toward the design of dynamically similar artificial insect wings. *International Journal of Micro Air Vehicles, 13*, 23–42. https://doi.org/10.1177/1756829321992138
31. Qiu, X. Q., Zhang, M. G., Jing, W. X., & Gao, C. S. (2021). Dynamics and adaptive sliding mode control of a mass-actuated fixed-wing uav. *International Journal of Aeronautical and Space Sciences, 22*, 886–897. https://doi.org/10.1007/s42405-020-00344-w
32. Chen, L., Zhang, Y. L., Chen, Z. Y., Xu, J., & Wu, J. H. (2020). Topology optimization in lightweight design of a 3d-printed flapping- wing micro aerial vehicle. *Chinese Journal of Aeronautics, 33*(12), 3206–3219. https://doi.org/10.1016/j.cja.2020.04.013
33. Sun, J. Y., Liu, C., & Bhushan, B. (2019). A review of beetle hindwings: structure, mechanical properties, mechanism and bioinspiration. *Journal of the Mechanical Behavior of Biomedical Materials, 94*, 63–73. https://doi.org/10.1016/j.jmbbm.2019.02.031

34. Addo-Akoto, R., Han, J.-S., & Han, J.-H. (2021). Roles of wing flexibility and kinematics in flapping wing aerodynamics. *Journal of Fluids and Structures, 104*, 103317. https://doi.org/10.1016/j.jfluidstructs.2021.103317
35. Song, Z. L., Tong, J., Yan, Y. W., & Sun, J. Y. (2020). Effects of pterostigma structure on vibrational characteristics during flight of asian ladybird *Harmonia Axyridis* (coleoptera: Coccinellidae). *Scientific Reports, 10*(1), 11371. https://doi.org/10.1038/s41598-020-68384-6
36. Zhang, Z. J., Sun, X. W., Du, P. Y., Sun, J. Y., & Wu, Y. F. (2018). Design of a hydraulically-driven bionic folding wing. *Journal of the Mechanical Behavior of Biomedical Materials, 82*, 120–125. https://doi.org/10.1016/j.jmbbm.2018.03.024
37. Liu, C., Li, P. P., Song, F., StamhuisEize, J., & Sun, J. Y. (2022). Design optimization and wind tunnel investigation of a flapping system based on the flapping wing trajectories of a beetle's hindwings. *Computers in Biology and Medicine, 140*, 105085. https://doi.org/10.1016/j.compbiomed.2021.105085
38. Yan, Y. W., & Sun, J. Y. (2022). Vibration modal characteristics analysis of bionic flapping wing based on hindwing of beetle. *Aeronautical Science & Technology, 33*, 81–87. https://doi.org/10.19452/j.issn1007-5453.2022.10.010
39. Sun, J. Y., Yan, Y. W., Li, F. D., & Zhang, Z. J. (2021). Generative design of bioinspired wings based on deployable hindwings of anomala corpulenta motschulsky. *Micron, 151*, 103150. https://doi.org/10.1016/j.micron.2021.103150
40. Dada, M., Popoola, P., Adeosun, S., & Pityana, S. (2021). Investigating the elastic modulus and hardness properties of a high entropy alloy coating using nanoindentation. *International Journal of Lightweight Materials and Manufacture, 4*, 339–345. https://doi.org/10.1016/j.ijlmm.2021.04.002
41. Zhao, C., Guo, H. H., Zhang, D., Liu, R. Q., Li, B., & Deng, Z. Q. (2020). Stiffness modeling of n(3RRlS) reconfigurable series-parallel manipulators by combining virtual joint method and matrix structural analysis. *Mechanism & Machine Theory, 152*, 103960. https://doi.org/10.1016/j.mechmachtheory.2020.103960
42. Shi, Y. B., Zhang, J. J., Jiao, J. J., Zhao, R., & Cao, H. L. (2021). Calibration analysis of high-g mems accelerometer sensor based on wavelet and wavelet packet denoising. *Sensors, 21*(4), 1231. https://doi.org/10.3390/s21041231
43. Wang, X. P., Huang, S. X., Kang, C., Li, G. Q., & Li, C. F. (2020). Integration of wavelet denoising and hht applied to the analysis of bridge dynamic characteristics. *Applied Sciences, 10*, 3605. https://doi.org/10.3390/app10103605